1 **Microfiltration Membranes Modified by Silver-decorated Biomimetic**

2 **Silica Nanopollens for Mitigating Biofouling: Synergetic Effects of**

3 **Nanopollens and Silver Nanoparticles**

4

5 Xingran Zhang [1], Meng Ping [1], Zhichao Wu [1], Chuyang Y. Tang [2], Zhiwei Wang [1,*]

6

7 [1] State Key Laboratory of Pollution Control and Resource Reuse, Shanghai Institute of

8 Pollution Control and Ecological Security, School of Environmental Science and

9 Engineering, Tongji University, Shanghai 200092, China

10 [2] Department of Civil Engineering, the University of Hong Kong, Pokfulam Road,

11 Hong Kong S.A.R., China

12 *Corresponding author. E-mail: zwwang@tongji.edu.cn

13

14

15

18

19

20

21

22

23

Abstract

Applications of membrane technologies for water and wastewater treatment call for antibiofouling membranes. Inspired by nature's spiky topological features of pollen grains, we developed silver-decorated biomimetic silica nanopollens (SNPs) to modify a polyvinylidene fluoride microfiltration membrane. The modified membrane demonstrated compelling antibiofouling performance compared to the pristine membrane, which was attributed to the synergetic effects of SNPs and loaded silver nanoparticles. The surface spikes of SNPs could act as multiple 'entry claws' to bind to the cell membrane upon contact, inducing physical deformation and metabolic disturbance of cells. More importantly, the SNPs could serve as a delivery vector for silver ions that were released from silver nanoparticles loaded in SNPs, further leading to cell damage due to the generation of reactive oxygen species and respiratory inhibition. These synergetic effects of SNPs and loaded silver nanoparticles imparted the modified membrane with potent antibiofouling behavior both in batch and continuous flow tests using model bacteria, *Escherichia coli* (Gram-negative) and *Staphylococcus aureus* (Gram-positive), respectively. Our strategy provides a novel pathway using biomimetic materials to fabricate antibiofouling membranes for water and wastewater treatment.

Keywords: Membrane biofouling; silica nanopollens; silver nanoparticles; polyvinylidene fluoride membrane; wastewater treatment

1. Introduction

Membrane technology is considered to be a promising technology for water and wastewater treatment [1, 2]. However, membrane fouling, particularly biofouling, remains as a bottleneck for the applications of membrane technology [3, 4]. Biofouling, *i.e.*, the attachment of bacteria and the growth of biofilm on the membrane surface, can result in remarkable water permeability decline [5, 6]. Several strategies have been developed for biofouling mitigation including feed pretreatment [7], membrane cleaning [8] and membrane surface modification [9, 10]. Among them, construction of biofouling-resistant membrane surfaces is an attractive protocol in tackling biofouling [11].

Recently, nature's creations have inspired researchers to develop biomimetic antibiofouling membranes. It has been reported that surface-coating of biomimetic materials could impart the membranes with antiadhesive ability. For instance, polydopamine (PDA), with a molecular structure similar to the sticky substances found in mussels, is a favorable agent for surface modification due to its strong hydrophilic nature [12-14]. However, this simple coating method could potentially block membrane pores [15]. Another biomimetic modification strategy is to modify the intrinsic structure of membranes. It has been reported that the incorporation of aquaporins [16] into membrane structure to create water channels could significantly increase membrane permeability. Under same membrane flux operation, the enhanced permeability of modified membranes facilitates mitigating membrane biofouling compared to the control [17]. However, these scenarios fail to impart membrane with bacteria-killing effects, and the membranes may still encounter severe membrane biofouling during long-term operation. A more attractive way is to construct membranes with a functionalized antimicrobial surface. Although the use of engineered nanoparticles,

74 such as Ag-nanoparticles (AgNPs) and Cu-nanoparticles (CuNPs), and antimicrobial

75 organics (*e.g.*, quaternary ammonium compounds) have been widely reported [18-20],

76 limited progress has been made using nature-derived biomimetic materials to impart

77 membranes with efficient bacteria-killing function.

78 Inspired by nature's materials with spiky topological features, such as pollen

79 grains [21-23], we developed silver-decorated biomimetic silica nanopollens (SNPs) to

80 modify polyvinylidene fluoride (PVDF) microfiltration membranes. We hypothesize

81 that silica nanopollens, with numerous nanosized spikes on the outer shell, interacts

82 strongly with bacterial cell membrane and causes physical disruption of the lipid bilayer

83 as well as metabolic disturbance of bacteria. At the meantime, the SNPs could act as a

84 delivery vector of AgNPs for direct release of silver ions inside the cell, leading to an

85 efficient biocidal behavior. These synergetic effects could impart the modified

86 membrane with potent antibiofouling behaviors due to the combination of contact-

87 killing (SNPs) and release-killing (AgNPs).

88 We elucidate the hypothesis in the present work by examining the antibiofouling

89 properties of the modified membranes using model bacteria, *Escherichia coli* and

90 *Staphylococcus aureus*, in both batch and continuous flow tests. Key questions

91 addressed in this work involve: (i) whether silver nanoparticles could be effectively

92 loaded into SNPs, (ii) what about the detailed role of spikes on the SNPs in causing

93 stress on bacteria, and (iii) what scenario is likely prevailing for SNPs and loaded

94 AgNPs to have the synergetic effects for mitigating biofouling of the modified

95 membrane.

96

97 **2. Materials and Methods**

98 **2.1 Materials and Reagents**

99　　　Unless specified otherwise, all chemicals were of analytic reagent grade.

100　Commercial grade PVDF (Solef® 6020, Mw=670–700 kDa) was received from Solvay.

101　Dimethylacetamide (DMAC) and dimethyl sulfoxide (DMSO) were used as solvents

102　and polyethylene glycol (PEG 400) as a pore-forming additive, all of which were

103　obtained from Sinopharm (China). Resorcinol, formaldehyde, ammonia aqueous

104　solution and tetraethyl orthosilicate (TEOS) were purchased from Sigma-Aldrich for

105　silica nanopollens preparation. Silver nitrate ($AgNO_3$, Sigma Aldrich) was used as the

106　silver source for the formation of AgNPs. All solutions were prepared using deionized

107　water.

2.2 Synthesis and Characterization of Silica Nanopollens and Ag-decorated Silica

Nanopollens.

110　　　Silica nanopollens (SNPs) were synthesized according to Stöber method [21].

111　Briefly, resorcinol (0.15 g) and formaldehyde (37 wt.%, 0.21 mL) were dissolved in the

112　mixture of ammonia aqueous solution (28 wt.%, 3.0 mL), deionized water (10 mL) and

113　ethanol (70 mL). The mixture was stirred for 6 h at room temperature, and then 0.6 mL

114　of TEOS was added into the solution and stirred for 8 min, followed by addition of

115　resorcinol (0.4 g) and formaldehyde (37 wt.%, 0.56 mL) and then 2 h stirring. The

116　products were collected by centrifugation, ethanol-washing and drying at 50°C. Finally,

117　SNPs were obtained after calcination at 550°C for 5 h in air. The schematic illustration

118　of the preparation procedures can be found in Supporting Information (SI) Fig. S1.

119　　　To load AgNPs on the surface of silica nanopollens, Ag-SiO_2 synthesis method

120　was used according to the literature [24]. In brief, silver nitrate (8.83 mmol) was added

121　into silica nanopollens slurry (50 mmol in 200 mL water) with ammonia solution (105

122　mmol) as a catalyst, and then the mixture was stirred for 6 h at room temperature. The

123　harvested products, *i.e.*, SNPs with loaded AgNPs (ASNPs), were purified by washing

with deionized water and then dried at room temperature for 2 h. Silver decoration mechanisms for silica nanoparticles are documented in SI Section S1.

The microstructures of SNP and ASNP samples were observed using field emission transmission electron microscopy (TEM) (JEOL, JEM-2100F, Japan). X-Ray photoelectron spectroscopy (XPS) (Thermo Scientific K-Alpha$^+$, USA) was used to determine the compositions of the specimens. The surface areas of the powders were determined using the Brunauer-Emmett-Teller (BET) (Micromeritics ASAP 2460, USA) with N_2 as adsorbate gas. The Ag loading mass of ASNP was measured by Inductively Coupled Plasma Optical Emission Spectrometer（ICP-OES, Agilent 720ES, USA）

2.3 Membrane Preparation and Characterization

Membranes were prepared by a phase inversion via immersion precipitation method. The casting solution of PVDF membrane was prepared as follows: PVDF (8 wt.%) and PEG (8 wt.%) were dissolved in a solvent mixture comprised of 42 wt.% DMAC and 42 wt.% DMSO at 80°C under stirring for 4 d. Afterward, a steel knife (250 μm clearance) was used to spread casting solution on polyester non-woven fabrics and then immersed into coagulation bath containing 200 mg/L SNPs or ASNPs. Teow et al [25, 26] found that nanoparticles were successfully embedded on the membrane surface through this method. The resulting SNPs and ASNPs modified PVDF membrane were denoted as SNP-M and ASNP-M, respectively. The pristine PVDF membrane (termed M0), without the presence of SNPs or ASNPs, was used as a control.

The membrane surface and cross-section morphologies was observed using field emission scanning electron microscopy (SEM) (Hitachi, S-4800, Japan) and atomic force microscopy (AFM) (Nanonavi E-Sweep, Japan). Elemental compositions of the membrane surface were determined by XPS. Surface hydrophilicity was determined by

149 the water sessile drop method. Water permeability was measured according to the

150 protocol described elsewhere [27]. Zeta potential of the membrane surface was

151 determined by a streaming potential analyzer (EKA1.00, Anton-Paar, Austria) at a

152 solution ionic strength of 10 mM KCl. The pore size of membranes was investigated

153 by a capillary flow porometer (Proplux, Porometer, USA). The Ag loading mass of

154 ASNP was measured by Inductively-Coupled Plasma Mass Spectrometry (ICP-MS,

155 Agilent 7700, USA)

156 **2.4 Antibacterial Activity Tests**

157 Gram-positive *Staphylococcus aureus* (*S. aureus*, ATCC25922) and Gram-

158 negative *Escherichia coli* (*E. coli*, ATCC6538) were used as the model bacteria.

159 Membrane coupons were immersed into the cells suspension (10^7 cells/mL in Davis

160 minimal medium) that was incubated on a rotary shaker for 12 h at 37°C. Viable cells

161 in the suspension were quantified using the colony forming unit (CFU) method [28].

162 Each value was shown by averaging triplicate measurements. The morphological

163 characteristics of the bacterial cells attached to the membrane surfaces after 12 h

164 incubation were examined by SEM.

165 The diffusion inhibition zone method was also used to evaluate the antibacterial

166 behaviors of the modified membrane [29]. In detail, 100 μL bacterial suspension was

167 spread on the agar plates. Membrane coupons were placed on the agar plates and

168 incubated at 37°C for 12 h. The diffusion inhibition zone formed around membranes

169 was determined by visual observation.

170 **2.5 Membrane Biofouling Experiments**

171 Dynamic biofouling experiments for membrane coupons (each with an effective

172 surface area of 40 cm^2) were performed in a cross-flow filtration reactor with an

173 effective volume of 7.2 L (see more details in SI Fig. S2). A saline containing *E. coli*

174   (10^5 cells/mL) and CH$_3$COONa (50 mg/L) was used as feed solution at pH of 7.4. The

175   system was operated for over 100 h at permeate flux of 42 L/(m^2 h) and temperature of

176   25 ± 1°C under continuous stirring (200 rpm). The membrane modules were subject to

177   2 h backwashing of DI water to remove foulants from membrane surfaces after 50 h

178   operation. In the end, membrane coupons (each with surface area of 1 cm^2) were cut

179   from the biofouled membrane, stained with SYTO 9, propidium iodide (LIVE/DEAD

180   BacLight Bacterial Viability Kits, Molecular Probes) and Concavalin A (Con A,

181   Molecular Probes) to respectively label viable/dead cells and extracellular polymeric

182   substances (EPS), and then mounted in a custom-made chamber for confocal laser

183   scanning microscopy (CLSM) (Nikon A1, Japan) observation. Image analysis was

184   performed using NIS-Elements Viewer and Photoshop software.

185   **2.6 Evaluation of Antibiofouling Mechanisms**

186   To investigate antibiofouling mechanisms, *E. coli* was incubated overnight with

187   silica nanopollens and Ag-decorated silica nanopollens (1 wt.%) in LB medium. The

188   particle-bacteria adhesion was directly observed with SEM after bacteria fixation and

189   staining. The integrity of the bacterial cell membranes was also evaluated by staining

190   the cells with SYTO 9 and propidium iodide (LIVE/DEAD BacLight Bacterial Viability

191   Kits). The silica nanospheres (SNSs), *i.e.*, without spikes, and Ag-decorated silica

192   nanospheres (ASNSs) were taken as control samples, with preparation procedures

193   shown in SI Section S2 and Fig. S1. The production of intracellular reactive oxygen

194   species (ROS) and adenosine triphosphate (ATP) by bacteria upon exposure to silica

195   and Ag-decorated silica was measured by ROS and ATP detection kit (Beyotime

196   Biotechnology, China), respectively. More details for ROS and ATP detection can be

197   found in SI Section S3.

198   AFM was used to measure the interactions between SNS/SNP and *E. coli*. Prior to

AFM observation, the SiN probe (Bruker, SNL-10, k = 0.06 N/m) was functionalized with SNS and SNP, respectively. In brief, AFM probes were precut to form a platform [30] and then adhered by SNS/SNP (Fig. S3) using correlative microscopy (Tescan, GAIA3 GMU Model 2016, Czech) combining focused ion beam and scanning electron microscopy (FIB-SEM) with Time-of-Flight Secondary Ion Mass Spectrometry (TOF-SIMS). A layer of Pt was deposited as glue to fix SNS/SNP onto the probe using the I-beam at 30 kV, 100 pA [30]. Ultimately, one SNS or SNP particle was immobilized on the probe (Fig. S3). Before contacting with SNS/SNP modified AFM probes, *E. coli* suspension (~10^8 cells/mL) was dripped to adhesion microscope slides (treated by polyethyleneimine) for 2 h [31]. Force-versus-distance curves were obtained in Peak Force Quantitative Nanomechanical Mapping (PF-QNM) mode with force loading rate of 48,000 pN/s (1 Hz of ramp rate, 800 nm of ramp size). The unbinding events are indicated by the sawtooth pattern in the retraction force curve [32]. The unbinding force histograms were compiled from ~50 force curves and were fitted with the Gaussian function.

Antibacterial efficiency of ASNS and ASNP was further determined using the following procedures. First, they were dialyzed in 0.5 mL batches against 13.6 mL dialysis water with different time vibrated at 150 rpm (Slide-A-Lyzer Mini Dialysis Devices, Thermofisher). The soaking solution was replaced daily and analyzed for their Ag^+ content with ICP-MS. The dialyzed samples were then collected and dosed into the *E. coli* suspension (10^7 cells/mL in Davis minimal medium) with different concentrations, and the mixture was incubated on a rotary shaker for 12 h at 37°C. Viable cells in the suspension were quantified using the colony forming unit (CFU) method.

**3. Results and Discussion**

3.1 Characterization of Silica Nanopollens, Ag-decorated Silica Nanopollens and Modified Membranes

TEM images show that the as-prepared silica nanopollens (SNPs) have numerous spikes on their surface (Fig. 1A). It can be observed that the SNP has a diameter of 230~240 nm, with an inner hollow cavity (92 nm in diameter) and a shell (30 nm in thickness) covered with nanosized silica spikes (average length of 40 nm). Due to its large external surface area (BET surface area of 88.0 m^2/g) and the unique structure, silica nanopollens provide a large quantity of sites for Ag loading. The N_2 adsorption and desorption show a typical type IV isotherm (Fig. S4) with the corresponding Barret-Joyner-Halenda (BJH) pore size of 9.0 nm (Fig. S4), similar to the distance between two adjacent spikes observed from TEM images.

After AgNPs were loaded, additional fine particles appeared on the silica shells and spikes (Fig. 1B). A dense shell with 55 nm thickness was observed, suggesting that AgNPs were well loaded on SNPs. High-resolution TEM (HRTEM) images revealed a lattice fringe spacing of 0.23 nm (Fig. 1C), corresponding to (111) planes for silver. Elemental analysis by EDX (inset of Fig. 1C) and XPS (Fig. 1D) confirmed that these nanoparticles were AgNPs [33]. In order to show AgNP distribution on SNP clearly, TEM images of one silver decorated silica nanopollen particle with different magnification are shown in SI Fig. S5. In addition, size distribution of AgNPs was analyzed using Image-J software (Fig. S6) and the loading mass of AgNPs in ASNP was determined to be ~21.3 wt.% by ICP-OES. The immobilization of AgNPs on the silica can be attributed to the reductive -OH groups on the silica nanopollens surface [24]. Nucleophiles were produced in alkaline condition via deprotonating hydroxyl ligands (-OH) on SNPs [34], and then these nucleophilic parts (-O-) could react with

249   electrophilic Ag^+ for generation of AgNPs.
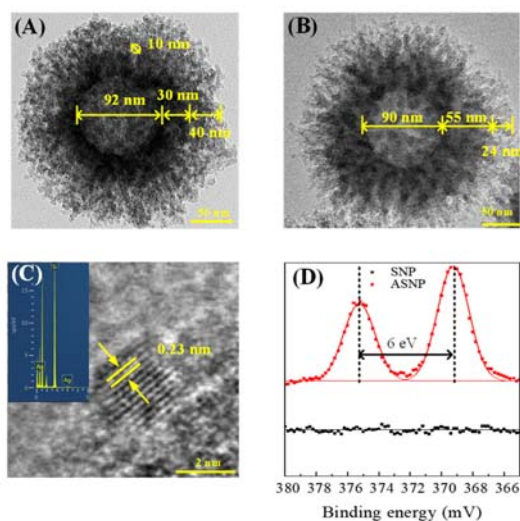
250

Fig. 1. TEM images of (A) SNP and (B) ASNP. (C) HRTEM lattice-fringe finger printing of the ASNP, with the corresponding EDS spectrum in the inset of the micrograph. The inter planar spacing (0.23 nm) is consistent with the crystal face of element silver. (D) Ag 3d spectra of SNP and ASNP.

255

Figs. 2A-C and Fig. S7 present the surface morphology and cross-section SEM images of the control membrane M0, the silica nanopollens modified membrane (SNP-M) and silver-decorated silica nanopollens modified membrane (ASNP-M). M0 had a porous surface structure with a pore size ~100 nm (inset of Fig. 2A). For SNP-M and ASNP-M, additional nanoparticles were clearly observed on the membrane surfaces, which were confirmed to be SNPs and ASNPs, respectively, based on XPS analysis (Fig. S8). Capillary flow porometer results (Fig.2D) show that the pore size of the three membranes had no significant difference (~100 nm). The loading mass of AgNPs in ASNP-M was determined to be ~107 μg/cm^2 by ICP-MS.

Fig. 2E shows that the contact angle of the modified membranes reduces from 75.1 ± 1.9° to 63.4 ± 1.3°, attributed to the presence of hydrophilic hydroxyl groups on SNPs

and ASNPs [35-37]. Compared to the control (46.8 ± 4.5 L/(m² h kPa)), the water permeability (Fig. 2F) was significantly increased to 63.4 ± 1.3 L/(m² h kPa) and 58.1 ± 6.4 L/(m² h kPa) for SNP-M and ASNP-M, respectively. Fig. 2G shows that the membrane surface charge was altered due to the introduction of SNPs and ASNPs: -30.4 ± 1.9 mV for M0, -36.1 ± 0.1 mV for SNP-M, and -32.7 ± 5.2 mV for ASNP-M at pH = 7.4. The negatively charged hydroxyl groups of SNP was the major reason causing the change of zeta potential of SNP-M [38]. However, with the formation of AgNPs on the silica nanopollens, hydroxyl groups were replaced by Si-O-Ag, impairing the negative zeta potential. For pollutant rejection behaviors, no significant difference in sodium alginate rejection was observed for the modified membranes compared to the control (Fig. S8).
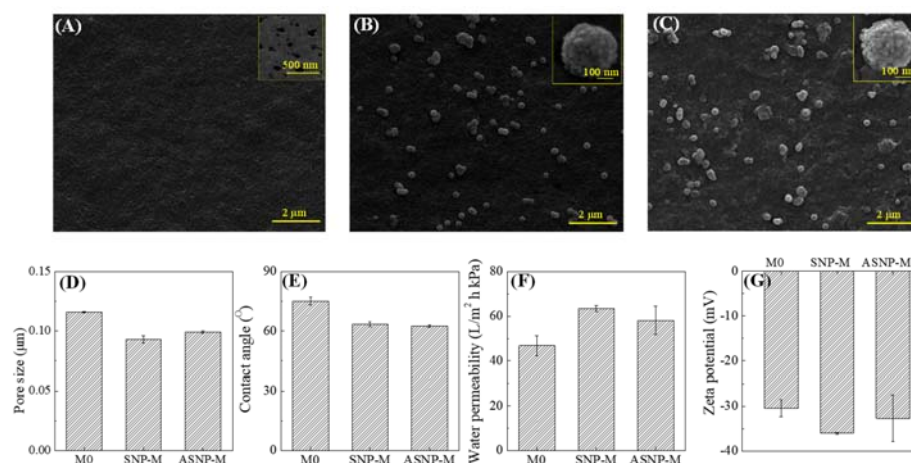
Fig. 2. SEM images of (A) M0, (B) SNP-M and (C) ASNP-M. The higher magnification micrographs are shown in the inset of each image. (D) Pore size (n=3), (E) contact angle of DI water on membranes ($n = 7$), (F) water permeability ($n = 3$) and (G) zeta potential ($n = 3$) of M0, SNP-M and ASNP-M.
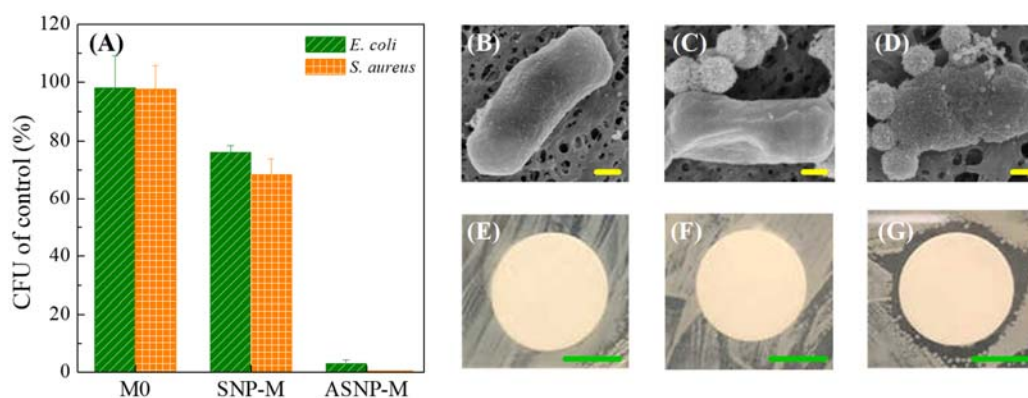
3.2 Antibacterial Activity Tests

Pristine and modified membranes were immersed in LB medium and incubated

with *E. coli* and *S. aureus* for 12 h. After incubation, the number of viable cells in the suspension was determined by the plate counting method. Compared to M0, CFU of SNP-M was decreased to 76.1% ± 2.3% for *E. coli* and 68.4% ± 5.4% for *S. aureus* (Fig. 3A), respectively. In contrast, the ASNP-M membrane exhibited more significant antibacterial performance, with CFU decreased to 3.0% ± 1.2% and 0.5% ± 0.1% for *E. coli* and *S. aureus* (Fig. 3A), respectively. This implies that the antibacterial effects are associated with not only AgNPs but also SNPs. SEM observations on membranes with attached bacteria further confirmed antibacterial behaviors. As shown in Fig. 3B, no apparent change in morphology of bacteria was observed for the M0 membrane. Compared with the pristine membrane, some of silica nanopollens on the SNP-M membrane surface were partially engulfed into the cell membrane of *E. coli,* resulting in severe deformation of cells (Fig. 3C). Further investigation by staining the cells with SYTO 9 and propidium iodide reveals cell membrane lesions to the majority of the cells upon their exposure to SNPs (Fig. S9). In contrast, this phenomenon did not occur for the case of SNSs. These results imply that the nanospikes of SNPs can physically puncture cell membranes to cause severe damages, which is analogous to the piercing of cell membranes by graphene oxide nanosheets [39]. Notably, the ASNP-M membrane caused a significant disruption of cell integrity (Fig. 3D), suggesting that AgNPs modification of SNPs can ensure effective antimicrobial activity. For the case of ASNPs, the piercing of cell membranes by nanospikes may compromise membrane integrity and allow Ag^+ from the AgNPs to be more effectively released inside the bacteria cell, a synergistic effect that will be further investigated under the section *Antibiofouling Mechanisms*.

Diffusion inhibition zone tests clearly demonstrate the antibacterial behaviors of SNP-M and ASNP-M. An inhibition circle formed around a specimen indicates

13

antibacterial activity based on the leaching effect of the antibacterial substance [29]. As expected, the pristine and silica nanopollens modified membrane did not show the formation of the inhibition circle toward *E. coli* and *S. aureus* (Figs. 3E and F, Figs. S10), revealing that the prevailing antibacterial effect imparted by SNPs was not associated with release killing (release of the antibacterial substance). In contrast, the AgNPs loading led to the formation of the inhibition zone toward *E. coli* and *S. aureus* (Fig. 3G and Fig. S10), indicating that leaching Ag^+ contributed to the antibacterial effects of ASNP-M.

Fig. 3. Antimicrobial properties (A) in terms of CFU of M0, SNP-M and ASNP-M after exposure to *E. coli* and *S. aureus* cells in Davis minimal medium for 12 h at 37°C. The antimicrobial activity was determined as the percentage of CFU relative to that on medium without membranes (control). SEM images reveal the morphological characteristics of *E. coli* on (B) M0, (C) SNP-M and (D) ASNP-M. Diffusion inhibition zone test of (E) M0, (F) SNP-M and (G) ASNP-M for Gram-negative *E. coli* bacteria. The yellow and green scale bar is 200 nm and 4 mm, respectively.

3.3 Membrane Biofouling Experiments
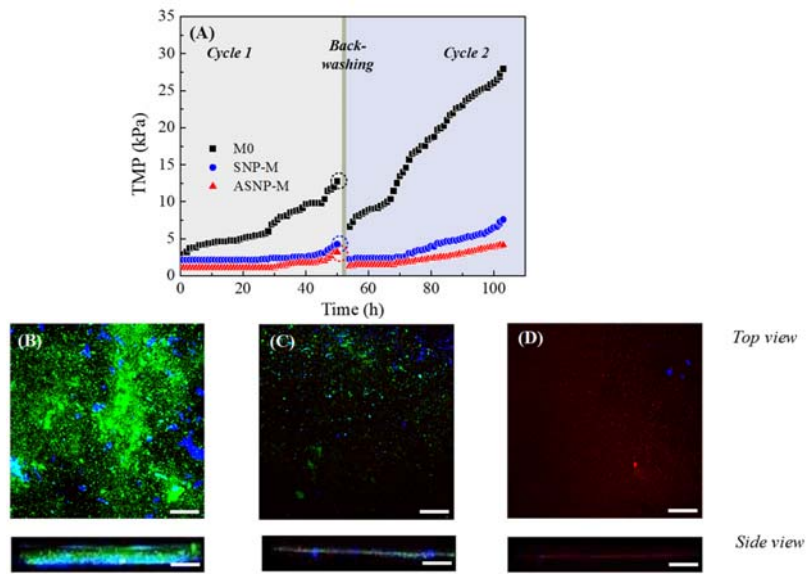
Antibiofouling behaviors were investigated in a cross-flow filtration reactors using *E. coli* suspension (10^5 cells/mL of initial concentration) as feed solution. Consistent

14

with the batch antibacterial tests, SNP-M and ASNP-M membranes exhibited a much

better performance against biofouling (Fig. 4A). Furthermore, the TMP increase rate of

ASNP-M membranes was lower compared to that of SNP-M, possibly due to the

synergetic effects imparted by silica nanopollens and AgNPs. A second fouling cycle

after a 2h-backwash with deionized water confirmed the same trend. Interestingly,

backwashing of SNP-M and ASNP-M after the first cycle restored the TMP almost back

to the original value, *i.e.*, 2.26 kPa/2.13 kPa (restored-TMP/original-TMP) for SNP-M

and 1.06 kPa/1.33 kPa for ASNP-M. In contrast, for M0, the TMP after membrane

cleaning (6.65 kPa) was much higher than the original value (2.66 kPa), which also

resulted in a rapid TMP increase in the second cycle due to subsequent severe

biofouling [40, 41]. The results demonstrated that the introduction of silica nanopollens

on the membrane surface enabled a better permeability recovery upon cleaning

compared to the control.

　　To understand the role of SNP and ASNP in biofouling mitigation, the fouled

membrane was removed from bioreactor at the end of operation cycle and stained for

CLSM analysis. Representative side and top views of the membranes are shown in Fig.

4B-D. The biovolumes of live cells, dead cells and EPS in biofilm are shown in Table

1. The results exhibit that the biofilm formed on SNP-M and ASNP-M was much

thinner and composed of fewer live cells, more dead cells and less EPS biovolumes

than the biofilm formed on the M0 membrane. Notably, most microorganisms in biofilm

on ASNP-M were dead with few cells alive. In contrast, the relative abundance of viable

cells and EPS of SNP-M was higher than that of ASNP-M, consistent with the results

presented in Fig. 3A.

　　Despite the interaction between silica nanopollens (numerous spikes) and bacterial

cells, the antiadhesive properties of SNP-M and ASNP-M membranes did not

deteriorate obviously (Table 1), which should be attributed to the improved intrinsic membrane properties and antibacterial ability imparted by silica nanopollens. For instance, the enhanced hydrophilicity and more negative zeta potential of membrane surface decreased the adhesion of organic foulants and bacteria onto membrane (Fig. 2E and G). Furthermore, a better TMP recovery for SNP-M and ASNP-M (Fig. 4A) after back flushing indicates a great potential of the modified membrane for long-term operation.

Fig. 4. (A) TMP variations of M0, SNP-M and ASNP-M as a function of time in filtration experiments using artificial wastewater involving *E. coli* for two operation cycles, 50 h of each. CLSM top and side view images of the biofilms of (A) M0, (B) SNP-M and (C) ASNP-M membranes at the end of the operation. Biofilms were stained with SYTO 9 (green) and PI (red) for live and/or dead cells, and dead cells, respectively. The scale bar is 60 μm. The dashed circles in part A indicate water cleaning points using DI water for membrane cleaning.

Table 1. Biofilm characteristics of M0, SNP-M and ASNP-M membranes (*n*=3).

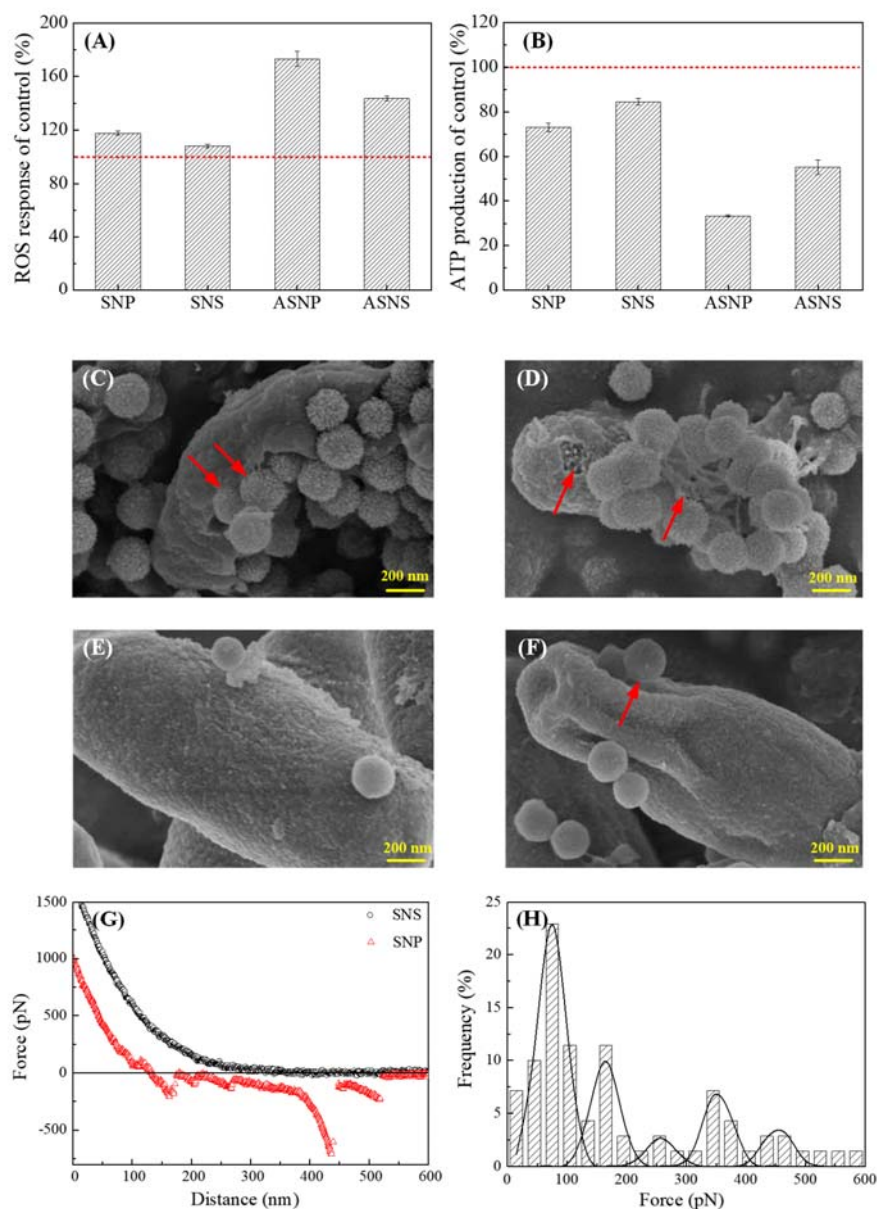| No.	Biofilm thickness (μm)	Live cell volume ($\mu m^3/\mu m^2$)	Dead cell volume ($\mu m^3/\mu m^2$)	EPS volume ($\mu m^3/\mu m^2$)
M0	66.0 ± 12.2	52.5 ± 10.8	0.7 ± 0.2	6.7 ± 1.5
SNP-M	22.0 ± 2.0	15.7 ± 3.9	3.5 ± 2.2	2.8 ± 1.2
ASNP-M	22.6 ± 1.2	0.2 ± 0.1	21.6 ± 1.8	0.9 ± 0.7

3.4 Antibiofouling Mechanisms

To further elucidate the underlying mechanisms, the accumulation of ROS was determined for *E. coli* upon exposure to SNPs, SNSs, ASNPs and ASNSs. As shown in Fig. 5A, intracellular ROS for SNPs was higher than that for SNSs, suggesting that the spikes of silica nanopollens in the solution phase could interact with the cells to induce increased production of ROS. Similarly, the ROS generation of ASNPs was higher than that of ASNSs, confirming the role of spikes in causing damage to bacteria. ATP production was inhibited for *E. coli* upon exposure to SNPs, SNSs, ASNPs and ASNSs (Fig. 5B). ATP activity of SNPs was decreased to 72.9% ± 2.0% compared to that of SNSs (84.5% ± 1.5%). Similarly, ASNPs had a lower ATP capacity (33.3% ± 0.4%) compared to ASNSs (55.2% ± 3.4%), suggesting that metabolism behaviors for ASNPs were more severely hindered.

To provide direct evidence on the antibiofouling mechanisms, SEM was employed to observe the morphology of *E. coli* after 12 h interaction with silica nanopollens and Ag-decorated silica nanopollens. It can be observed that silica nanopollens are partially embedded into the cell (Fig. 5C, indicated by the red arrows), inducing morphology deformation of bacteria, which is consistent with the result of membrane antibacterial test (Fig. 3B). For the Ag-decorated silica nanopollens, severe damage of bacteria can

17

be clearly observed on the bacterial surface from SEM image (Fig. 5D, indicated by the red arrows), which may result from the release of Ag^+ from AgNPs loaded on the silica nanopollens. In contrast, no obvious damage to bacterial cell was observed although silica nanospheres could attach to bacterial surfaces (Fig. 5E). Ag-decorated SNSs could cause deformation of cell due to the presence of AgNPs (Fig. 5F).


Fig. 5. (A) Intracellular ROS production and (B) ATP activity of *E. coli* upon exposure

to silica nanopollens (SNPs), silica nanospheres (SNSs) and their silver-decorated samples (ASNPs and ASNSs), n=3. The LB medium involving *E. coli* without samples was taken as a control. SEM images of (C) SNPs, (D) ASNPs, (E) SNSs and (F) ASNSs adhered on *E. coli* surface. (G) Force *vs* distance curves during retraction of SNP/SNS modified AFM probes from the substrate-supported *E. coli* bacteria measured in deionized water. (H) Unbinding force histogram measured in deionized water between the SNP modified AFM probe and the substrate-supported *E. coli* bacteria. The histogram was obtained from ∼50 force curves. The histogram was fitted by Gaussian distribution.

The role of surface spikes of silica nanopollens in interacting with bacteria was further revealed by AFM retraction force measurements. The binding affinity between SNS/SNP mounted on the AFM tip and the supported *E. coli* bacteria on adhesion microscope slides was analyzed by the retraction force curves. The sawtooth force pattern and its force histogram (Figs. 5G and H), associated with sequential unbinding events of multiple bonds disrupted in parallel [42, 43], suggests that there might exist multivalent interactions induced by SNP surface spikes in contact with the bacteria surface. In contrast, there was no attractive interactions between silica nanospheres and the supported cell membrane (Fig. 5G). This demonstrates that the damaged cell structure and metabolism behaviors caused by nanospikes are associated with specific multivalent attractive forces between surface spikes and cell membranes. In fact, multivalent topology (*e.g.*, star shape [44]) has been proven favorable for triggering receptor-mediated cellular uptake that can puncture pores on cell membranes causing damage to its function, such as cell signaling and communication as well as transportation of substances in and out [45].

425   Fig. 6 summarizes the antibiofouling mechanisms of ASNPs. The insertion of

426   nanospikes into cell membrane provides active sites for ROS-mediated oxidative stress

427   and causing ATP synthesis inhibition. Furthermore, the loaded AgNPs on the

428   nanopollens could dissolve to release Ag^+ inside the cell if the cell membrane suffered

429   lesions with a loss of integrity. These synergetic effects of silica nanopollens and AgNPs

430   promote efficient antimicrobial activity, leading to consequent inhibition of bacterial

431   growth and colonization on the membrane surface.

432
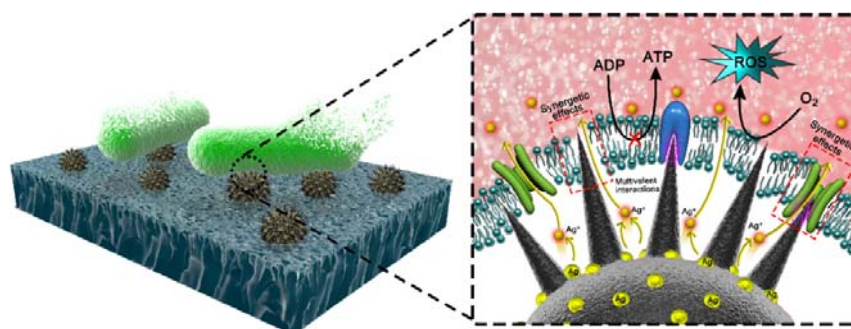
Fig. 6. A schematic representation of the antibiofouling behaviors of ASNP-M
434   membranes.

435

436   Fig. 7A presents silver release behaviors of ASNPs and ASNSs. ASNPs exhibited

437   lower initial Ag^+ release than ASNSs, which was possibly attributed to the accessible

438   inner cavity of mesostructured silica nanopollens favorable for controlling the Ag^+

439   release [46]. After 14 d exposure period, Ag^+ release rate of the both samples reached a

440   stable and similar value (~4 μg/d). Furthermore, the ASNPs showed a strong

441   antibacterial effects in terms of CFU reduction after 34 d exposure compared to ASNS

442   samples (Fig. 7B and C). This result indicates that the antibacterial effectiveness of

443   ASNPs was higher and more lasting than that of ASNSs, which should be attributed to

444   the synergetic effects of silica nanopollens and AgNPs to enhance the biocidal

445   efficiency.

446   While the presence of AgNPs is effective in antibiofouling application, the AgNPs

447   based membrane still have severe concerns on the potential of environmental risk [47].

448   It is likely that overuse of silver as biocides will result in increased silver resistance of

449   some microorganisms [48]. In this study, silica nanopollens provide a conducive

450   environment for Ag^+ release inside the bacterial cell to avoid ineffective release of Ag^+

451   and decrease their potential risk on environment, which provides a new dimension for

452   fabrication of antibiofouling membranes using AgNPs@silica nanopollens for water

453   and wastewater treatment.
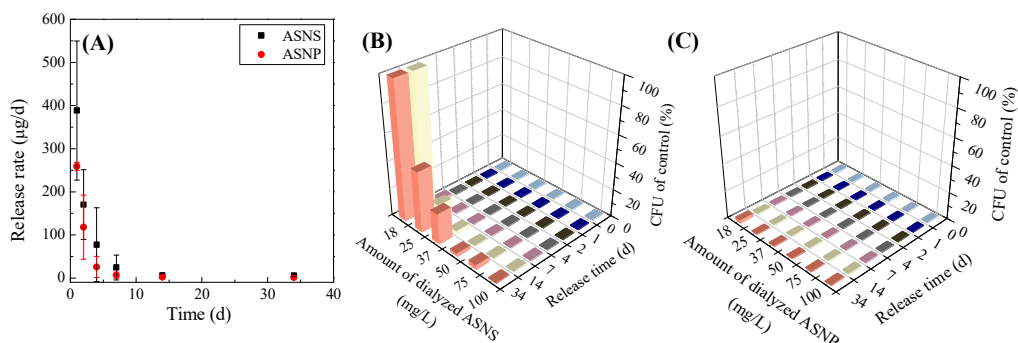
454

455   **Fig. 7.** (A) Release rate *vs* time of ASNS and ASNP. Quantification of antibacterial

456   efficiency as a function of release time of (B) ASNS and (C) ASNP on *E. coli*.

457

458   Antimicrobial properties based on contact-killing strategy have been imparted to

459   membranes to target biofouling, including the use of nanomaterials of contact-mediated

460   cytotoxicity [49, 50], quaternary ammonium compounds [10] and zwitterion polymer

461   brushes [51]. Notably, for nanomaterials-based strategy, direct physical toxicity only

462   occurs through intimate contact, implying that the antimicrobial efficiency is dependent

463   on the chance for mechanical disruption. Recent studies have shown that the intensity

464   of mechanical cell damage varies for nanomaterials with different topologies, such as

465   size, shape, orientation or dimensionality, and cytotoxicity could be enhanced if

reasonable topology is designed to provide more active sites for contacting [52-55]. In this study, a novel bio-inspired material with numerous nanospikes outside, *i.e.*, silica nanopollens, was developed to enhance antibiofouling efficiency of modified membranes. Compared to silica nanoparticles, silica nanopollens could pierce bacterial cell membrane via "needle-like" topology with three-dimensional (3D) macrostructure, which imparts more penetration sites per unit area to enhance physical cell damage. Besides, they provide a high surface-area platform for AgNPs loading and a conducive environment for Ag^+ release inside the bacterial cell to trigger severe cell toxicity. The synergetic effects ensure a stable and efficient antibiofouling performance for the modified membrane. This work introduces a new platform for design of antibiofouling surfaces using nanomaterials with the nanospikes structure.

The piercing effects caused by the nanopollens are somewhat similar that those observed for carbon nanotubes (1D materials) and GO nanosheets (2D materials) [52]. Indeed, these 1D and 2D carbon-based materials have been reported for the preparation of antibiofouling membranes. However, their use may require carefully alignment to expose their sharp edges, *e.g.*, by vertically aligning GO nanosheets [56, 57], which often greatly increases the cost and severely limits the scale of membrane production. In this regard, the 3D needle-like topology of nanopollens can offer a great advantage by avoiding this strict requirement of alignment. Despite the efficient antimicrobial performance demonstrated in the current study, the density, length and radius of nanospikes need to be further optimized. The importance of nanospikes 3D macrostructure for cell damage has implications for potential utilization of a wide range of metals or metal oxides with similar topology for membrane antibiofouling.

4. Conclusions

An antibiofouling polyvinylidene fluoride microfiltration membrane was fabricated by incorporating silver-decorated biomimetic silica nanopollens (SNPs). Attributed to the synergetic effects of SNPs and loaded silver nanoparticles, the modified membrane demonstrated compelling antibiofouling performance compared to the pristine membrane. The surface spikes of SNPs could act as multiple 'entry claws' to bind to the cell membrane upon contact, inducing damage to bacterial cells. Furthermore, the SNPs could serve as a delivery vector for silver ions that were released from silver nanoparticles loaded in SNPs, causing further damage to bacterial cells due to the generation of reactive oxygen species and respiratory inhibition. These synergetic effects of SNPs and loaded silver nanoparticles imparted the modified membrane with potent antibiofouling behavior.

ASSOCIATED CONTENT

Supporting Information

The Supporting Information is available free of charge on the Publications website.

Silver decoration mechanisms for silica nanoparticles (Section S1); Synthesis of silica nanospheres and silver-decorated silica nanospheres (Section S2); Experimental procedures for intracellular ROS and ATP tests (Section S3); Schematic illustration of SNP and SNS synthesis (Fig. S1); MBR experimental set-up (Fig. S2); Images of the AFM tips (Fig. S3); BJT pore size distribution (Fig. S4); TEM images of one silver decorated silica nanopollen particle with different magnification (Fig. S5); Size distribution of AgNPs on the silica nanopollen (Fig. S6); Cross-section SEM images (Fig. S7); XPS spectra, SA rejection and roughness of membranes (Fig. S8); CLSM

images of *E. coli* cells contacted with the SNPs and SNSs (Fig. S9). The formation of the inhibition zone toward *S. aureus* (Fig. S10).

AUTHOR INFORMATION

Corresponding Author

*E-mail: zwwang@tongji.edu.cn

Notes

The authors declare no competing financial interest.

References

[1] M. Elimelech, W. A. Phillip, The future of seawater desalination: Energy, technology, and the environment, Science 333 (2011) 712-717.

[2] A. G. Fane, R. Wang, M. Hu, Synthetic Membranes for Water Purification: Status and Future, Angew. Chem. Int. Edit. 54 (2015) 3368-3386.

[3] S. Jiang, Y. Li, B. P. Ladewig, A review of reverse osmosis membrane fouling and control strategies, Sci. Total. Environ. 595 (2017) 567-583.

[4] H. Lu, Z. Xue, P. Saikaly, S. P. Nunes, T. R. Bluver, W. Liu, Membrane biofouling in a wastewater nitrification reactor: Microbial succession from autotrophic colonization to heterotrophic domination, Water Res. 88 (2016) 337-345.

[5] L. H. Kim, T. H. Chong, Physiological Responses of Salinity-Stressed Vibrio sp. and the Effect on the Biofilm Formation on a Nanofiltration Membrane, Environ. Sci. Technol. 51 (2017) 1249-1258.

[6] C. Liu, A. F. Faria, J. Ma, M. Elimelech, Mitigation of Biofilm Development on Thin-Film Composite Membranes Functionalized with Zwitterionic Polymers and Silver Nanoparticles, Environ. Sci. Technol. 51 (2017) 182-191.

[7] J. S. Vrouwenvelder, F. Beyer, K. Dahmani, N. Hasan, G. Galjaard, J. C. Kruithof, M. C. M. van Loosdrecht, Phosphate limitation to control biofouling, Water Res. 44 (2010) 3454-3466.

[8] C. Marconnet, A. Houari, D. Seyer, M. Djafer, G. Coriton, V. Heim, P. Di Martino, Membrane biofouling control by UV irradiation. Desalination 276 (2011) 75-81.

[9] L. Qi, Y. Hu, Z. Liu, X. An, E. B. Zeev, Improved anti-biofouling performance of thin-film composite forward-osmosis membranes containing passive and active moieties, Environ. Sci. Technol. 52 (2018) 9684-9693.

[10] X. Zhang, J. Ma, C. Y. Tang, Z. Wang, H. Y. Ng, Z. Wu, Antibiofouling polyvinylidene fluoride membrane modified by quaternary ammonium compound: direct contact-killing versus induced indirect contact-killing. Environ. Sci. Technol. 50 (2016) 5086-5093.

[11] R. Zhang, Y. Liu, M. He, Y. Su, X. Zhao, M. Elimelech, Z. Jiang, Antifouling membranes for sustainable water purification: strategies and mechanisms. Chem. Soc. Rev. 45 (2016) 5888-5924.

[12] Z. Yang, Y. Wu, J. Wang, B. Cao, C. Y. Tang, *In situ* reduction of silver by polydopamine: a novel antimicrobial modification of a thin-film composite polyamide membrane. Environ. Sci. Technol. 50 (2016) 9543−9550.

[13] X. Zhang, Z. Wang, C. Y. Tang, J. Ma, M. Liu, M. Ping, M. Chen, Z. Wu,

Modification of microfiltration membranes by alkoxysilane polycondensation induced quaternary ammonium compounds grafting for biofouling mitigation. J. Membr. Sci. 549 (2018) 165-172.

[14] L. Tang, K. J. T. Livi, K. L. Chen, Polysulfone membranes modified with bioinspired polydopamine and silver nanoparticles formed in situ to mitigate biofouling. Environ. Sci. Technol. Lett. 2 (2015) 59-65.

[15] M. A. Shannon, P. W. Bohn, M. Elimelech, J. G. Georgiadis, B. J. Marinas, A. M. Mayes, Science and technology for water purification in the coming decades. Nature 452 (2008) 30-310.

[16] Y. Zhao, A. Vararattanavech, X. Li, C. HelixNielsen, T. Vissing, J. Torres, R. Wang, A. G. Fane, C. C. T. Tang, Effects of proteoliposome composition and draw solution types on separation performance of aquaporin-based proteoliposomes: implications for seawater desalination using aquaporin-based biomimetic membranes. Environ. Sci. Technol. 47 (2013) 1496-1503.

[17] X. Li, C. H. Loh, R. Wang, W. Widjajanti, J. Torres, Fabrication of a robust high-performance FO membrane by optimizing substrate structure and incorporating aquaporin into selective layer. J. Membr. Sci. 525 (2017) 257-268.

[18] Y. Bi, B. Han, S. Zimmerman, F. Perreault, S. Sinha, P. Westerhoff, Four release tests exhibit variable silver stability from nanoparticle-modified reverse osmosis membranes. Water Res. 143 (2018) 77-86.

[19] M. Ben-Sasson, K. R. Zodrow, G. Qi, Y. Kang, E. P. Giannelis, M. Elimelech, Surface functionalization of thin-film composite membranes with copper nanoparticles for antimicrobial surface properties. Environ. Sci. Technol. 48 (2014) 384-393.

[20] M. Ping, X. Zhang, M. Liu, Z. Wu, Z. Wang, Surface modification of polyvinylidene fluoride membrane by atom-transfer radical-polymerization of

quaternary ammonium compound for mitigating biofouling. J. Membr. Sci. 570 (2019) 286-293.

[21] H. Song, Y. Ahmad Nor, M. Yu, Y. Yang, J. Zhang, H. Zhang, C. Xu, N. Mitter, C. Yu, Silica Nanopollens Enhance Adhesion for Long-Term Bacterial Inhibition. J. Am. Chem. Soc. 138 (2016) 6455-6462.

[22] S. Barrier, A. Diego-Taboada, M. J. Thomasson, L. Madden, J. C. Pointon, J. D Wadhawan, S. T. Beckett, S. L. Atkin, G. Mackenzie, Viability of plant spore exine capsules for microencapsulation. J. Mater. Chem. 21 (2011) 975-981.

[23] R. W. Thorp, The collection of pollen by bees. Plant Syst. Evol. 222 (2000) 211-223.

[24] Y. H. Kim, D. K. Lee, H. G. Cha, C. W. Kim, Y. S. Kang, Synthesis and Characterization of Antibacterial Ag-SiO2 Nanocomposite. J. Phys. Chem. C 111 (2007) 3629-3635.

[25] Y. H. Teow, A.L. Ahmad, J.K. Lim, B.S. Ooi. Preparation and characterization of PVDF/TiO2 mixed matrix membrane via in situ colloidal precipitation method. Desalination 295 (2012) 61-69.

[26] Y.H. Teow, B.S. Ooi, A.L. Ahmad. Study on PVDF-TiO2 mixed-matrix membrane behaviour towards humic acid adsorption. Journal of Water Process Engineering 15 (2017) 99-106.

[27] S. Ren, C. Boo, N. Guo, S. Wang, M. Elimelech, Y. Wang, Photocatalytic Reactive Ultrafiltration Membrane for Removal of Antibiotic Resistant Bacteria and Antibiotic Resistance Genes from Wastewater Effluent. Environ. Sci. Technol. 52 (2018) 8666-8673.

[28] F. Perreault, M. E. Tousley, M. Elimelech, Thin-film composite polyamide membranes functionalized with biocidal graphene oxide nanosheets. Environ. Sci.

Technol. Lett. 1 (2014) 71-76.

[29] J. Nikkola, X. Liu, Y. Li, M. Raulio, H. L. Alakomi, J. Wei, C. Y. Y. Tang, Surface modification of thin film composite RO membrane for enhanced anti-biofouling performance. J. Membr. Sci. 444 (2013) 192-200.

[30] X. Zhang, Y. He, J. Liu, M. E. Bowden, L. Kovarik, S. X. Mao, C. Wang, J. J. De Yoreo, K. M. Rosso, Accessing crystal-crystal interaction forces with oriented nanocrystal atomic force microscopy probes. Nat. Protocols 13 (2018) 2005-2030.

[31] D. Alsteens, H. Trabelsi, P. Soumillion, Y. F. Dufrêne, Multiparametric atomic force microscopy imaging of single bacteriophages extruding from living bacteria. Nat. Commun. 4 (2013) 2926.

[32] Y. J. Oh, M. Hubauer-Brenner, H. J. Gruber, Y. Cui, L. Traxler, C. Siligan, S. Park, P. Hinterdorfer, Curli mediate bacterial adhesion to fbronectin via tensile multiple bonds. Sci. Rep. 6 (2016) 33909.

[33] F. Kang, P. J. Alvarez, D. Zhu, Microbial extracellular polymeric substances reduce Ag+ to silver nanoparticles and antagonize bactericidal activity. Environ. Sci. Technol. 48 (2014) 316-322.

[34] R. Sabia, L. Ukrainczyk, Surface chemistry of SiO2 and TiO2–SiO2 glasses as determined by titration of soot particles. J. Non-Cryst. Solids 277 (2000) 1-9.

[35] H. J. Song, C. K. Kim, Fabrication and properties of ultrafiltration membranes composed of polysulfone and poly(1-vinylpyrrolidone) grafted silica nanoparticles. J. Membr. Sci. 444 (2013) 318-326.

[36] S. H. Park, Y. S. Ko, S. J. Park, J. K. Lee, J. Cho, K. Y. Baek, I, T. Kim, K. Woo, J. H. Lee, Immobilization of silver nanoparticle-decorated silica particles on polyamide thin film composite membranes for antibacterial properties. J. Membr. Sci. 499 (2016) 80-91.

[37] J. Yin, Y. Yang, Z. Hu, B. Deng, Attachment of silver nanoparticles (AgNPs) onto thin-film composite (TFC) membranes through covalent bonding to reduce membrane biofouling. J. Membr. Sci. 441 (2013) 73-82.

[38] H. Yang, J. Pi, K. Liao, H. Huang, Q. Wu, X. Huang, Z. Xu, Silica-decorated polypropylene microfiltration membranes with a mussel-inspired intermediate layer for oil-in-water emulsion separation. ACS Appl. Mater. Interfaces 6 (2014) 12566-12572.

[39] F. Perrealt, A. F. de Faria, M. Elimelech, Environmental applications of graphene-based nanomaterials. Chem. Soc. Rev. 44 (2015) 5861-5896.

[40] G. Ye, J. Lee, F. Perreault, M. Elimelech, Controlled architecture of dual-functional block copolymer brushes on thin-film composite membranes for integrated "defending" and "attacking" strategies against biofouling. ACS Appl. Mater. Interfaces 7 (2015) 23069-23079.

[41] C. Liu, J. L. Lee, J. Ma, M. Elimelech, Antifouling thin-film composite membranes by controlled architecture of zwitterionic polymer brush layer. Environ. Sci. Technol. 51 (2017) 2161-2169.

[42] H. Handa, S. Gurczynski, M. P. Jackson, G. Mao, Immobilization and Molecular Interactions between Bacteriophage and Lipopolysaccharide Bilayers. Langmuir 26 (2010) 12095-12103.

[43] R. Merkel, P. Nassoy, A. Leung, K. Ritchie, E. Evans, Energy landscapes of receptor–ligand bonds explored with dynamic force spectroscopy. Nature 397 (1999) 50-53.

[44] X. Xu, Y. Li, Q. Liang, Z. Song, F. Li, H. He, J. Wang, L. Zhu, Z. Lin, L. Yin, Efficient gene delivery mediated by a helical polypeptide: controlling the membrane activity via multivalency and light-assisted photochemical internalization (PCI). ACS Appl. Mater. Interfaces 10 (2018) 256-266.

[45] C. Fasting, C. A. Schalley, M. Weber, O. Seitz, S. Hecht, B. Koksch, J. Dernedde, C. Graf, E. W. Knapp, R. Haag, Multivalency as a chemical organization and action principle. Angew. Chem. Int. Ed. 51 (2012) 10472-10498.

[46] Y. Song, H. Jiang, B. Wang, Y. Kang, J. Chen, Silver-incorporated mussel-inspired polydopamine coatings on mesoporous silica as an efficient nanocatalyst and antimicrobial agent. ACS Appl. Mater. Interfaces 10 (2018) 1792-1801.

[47] S. Aslan, C. Z. Loebick, S. Kang, M. Elimelech, L. D. Pfefferle, P. R. van Tassel, Antimicrobial biomaterials based on carbon nanotubes dispersed in poly(lactic-co-glycolic acid), Nanoscale 2 (2010) 1789–1794.

[48] S. Silver, L.T. Phung, G. Silver, J. Ind. Microbiol. Biotechnol. 33 (2006) 627-634.

[49] F. Perreault, H. Jaramillo, M. Xie, M. Ude, L. D. Nghiem, M. Elimelech, Biofouling mitigation in forward osmosis using graphene oxide functionalized thin-film composite membranes. Environ. Sci. Technol. 50 (2016) 5840-5848.

[50] A. Tiraferri, C. D. Vecitis, M. Elimelech, Covalent binding of single-walled carbon nanotubes to polyamide membranes for antimicrobial surface properties. ACS Appl. Mater. Interfaces 3 (2011) 2869-2877.

[51] C. Liu, A. F. Faria, J. Ma, M. Elimelech, Mitigation of biofilm development on thin film composite membranes functionalized with zwitterionic polymers and silver nanoparticles. Environ. Sci. Technol. 51 (2017) 182-191.

[52] Q. Xin, H. Shah, A. Nawaz, W. Xie, M. Z. Akram, A. Botool, L. Tian, S. U. Jan, R. Boddula, B. Guo, Q. Liu, J. R. Gong, Antibacterial carbon-based nanomaterials. Adv. Mater. 2018 1804838.

[53] X. Zou, L. Zhang, Z. Wang, Y. Luo, Mechanisms of the antimicrobial activities of graphene materials. J. Am. Chem. Soc. 138 (2016) 2064-2077.

[54] S. Aslan, C. Z. Leobick, S. Kang, M. Elimelech, L. D. Pfefferle, P. R. Van Tassel,

Antimicrobial biomaterials based on carbon nanotubes dispersed in poly(lactic-co-glycolic acid).Nanoscale 2 (2010) 1789-1794.

[55] J. Lee, S. Mahendra, P. J. J. Alvarez, Nanomaterials in the construction industry: A review of their applications and environmental health and safety considerations. ACS Nano 4 (2010) 3580-3590.

[56] X. Lu, X. Feng, X. Zhang, M. N. Chukwu, C. O. Osuji, M. Elimelech, Fabrication of a desalination membrane with enhanced microbial resistance through vertical alignment of graphene oxide. Environ. Sci. Technol. Lett. 5 (2018) 614-620.

[57] X. Lu, X. Feng, J. R. Werber, C. Chu, I. Zucker, J. Kim, C. O. Osuji, Enhanced antibacterial activity through the controlled alignment of graphene oxide nanosheets. Proc. Natl. Acad. Sci. USA 114 (2017) 9793-9801.

714

List of figure captions

Fig. 1. TEM images of (A) SNP and (B) ASNP. (C) HRTEM lattice-fringe finger printing of the ASNP, with the corresponding EDS spectrum in the inset of the micrograph. The inter planar spacing (0.23 nm) is consistent with the crystal face of element silver. (D) Ag 3d spectra of SNP and ASNP.

Fig. 2. SEM images of (A) M0, (B) SNP-M and (C) ASNP-M. The higher magnification micrographs are shown in the inset of each image. (D) Pore size (n=3), (E) contact angle of DI water on membranes ($n = 7$), (F) water permeability ($n = 3$) and (G) zeta potential ($n = 3$) of M0, SNP-M and ASNP-M.

Fig. 3. Antimicrobial properties (A) in terms of CFU of M0, SNP-M and ASNP-M after exposure to *E. coli* and *S. aureus* cells in Davis minimal medium for 12 h at 37°C. The antimicrobial activity was determined as the percentage of CFU relative to that on medium without membranes (control). SEM images reveal the morphological characteristics of *E. coli* on (B) M0, (C) SNP-M and (D) ASNP-M. Diffusion inhibition zone test of (E) M0, (F) SNP-M and (G) ASNP-M for Gram-negative *E. coli* bacteria. The yellow and green scale bar is 200 nm and 4 mm, respectively.

Fig. 4. (A) TMP variations of M0, SNP-M and ASNP-M as a function of time in filtration experiments using artificial wastewater involving *E. coli* for two operation cycles, 50 h of each. CLSM top and side view images of the biofilms of (A) M0, (B) SNP-M and (C) ASNP-M membranes at the end of the operation. Biofilms were stained with SYTO 9 (green) and PI (red) for live and/or dead cells, and dead cells, respectively. The scale bar is 60 μm. The dashed circles in part A indicate water cleaning points using DI water for membrane cleaning.

Fig. 5. (A) Intracellular ROS production and (B) ATP activity of *E. coli* upon exposure

32

to silica nanopollens (SNPs), silica nanospheres (SNSs) and their silver-decorated samples (ASNPs and ASNSs), n=3. The LB medium involving *E. coli* without samples was taken as a control. SEM images of (C) SNPs, (D) ASNPs, (E) SNSs and (F) ASNSs adhered on *E. coli* surface. (G) Force *vs* distance curves during retraction of SNP/SNS modified AFM probes from the substrate-supported *E. coli* bacteria measured in deionized water. (H) Unbinding force histogram measured in deionized water between the SNP modified AFM probe and the substrate-supported *E. coli* bacteria. The histogram was obtained from ∼50 force curves. The histogram was fitted by Gaussian distribution.

Fig. 6. A schematic representation of the antibiofouling behaviors of ASNP-M membranes.

Fig. 7. (A) Release rate *vs* time of ASNS and ASNP. Quantification of antibacterial efficiency as a function of release time of (B) ASNS and (C) ASNP on *E. coli*.

List of table captions

Table 1. Biofilm characteristics of M0, SNP-M and ASNP-M membranes (n=3).